

## Determining the Locations of Dust Sources in FeLoBAL Quasars

Jay P. Dunn<sup>1</sup>, Branden Wasik<sup>1</sup>, Christin L. Holtzclaw<sup>1</sup>, David Yenerall<sup>1</sup>, Manuel Bautista<sup>2</sup>,  
Nahum Arav<sup>3</sup>, Daniel Hayes<sup>1</sup>, Max Moe<sup>4</sup>, Luis C. Ho<sup>5,6</sup>, S. Harper Dutton<sup>1</sup>

Received \_\_\_\_\_; accepted \_\_\_\_\_

---

<sup>1</sup>Department of Physical Sciences, Georgia Perimeter College, Dunwoody, GA 30338,  
USA: jdunn@gpc.edu

<sup>2</sup>Department of Physics, Western Michigan University, Kalamazoo, MI 49008-5252, USA

<sup>3</sup>Department of Physics, Virginia Tech, Blacksburg, VA 24060, USA

<sup>4</sup>Harvard-Smithsonian Center for Astrophysics, 60 Garden Street, MS-10, Cambridge,  
MA, 02138, USA

<sup>5</sup>Kavli Institute for Astronomy and Astrophysics, Peking University, Beijing 100871,  
China

<sup>6</sup>The Observatories of the Carnegie Institution for Science, 813 Santa Barbara Street,  
Pasadena, CA 91101, USA

## ABSTRACT

We conduct a spectroscopic search of quasars observed by the Sloan Digital Sky Survey (SDSS) with broad absorption line (BAL) troughs due to Mg II and troughs due to Fe II that simultaneously exhibit strong Balmer narrow emission lines. We find that in a redshift range of  $0.4 \leq z \leq 0.9$  approximately 23 of the 70 Mg II BALs and 4 of a subset of 15 Fe II BALs exhibit strong Balmer emission. We also find significant fractions of Mg II BALs (approx. 23%) and those Mg II BALs with Fe II troughs (approx. 27%) have strong continuum reddening,  $E(B-V) \geq 0.1$ . From measurements of the Balmer decrement in three objects, we find similarly significant reddening of the narrow emission line region in 3 of the 4 objects; the narrow emission lines in the fourth object are not measurable. We also include one object in this study not taken from the SDSS sample that shows Fe II absorption and strong narrow emission, but due to measurement uncertainty and low continuum reddening the comparison is consistent but inconclusive. We find a trend in both the Mg II and Fe II BAL samples between the narrow emission line reddening and continuum reddening. Because the narrow line reddening is consistent with the continuum reddening in every object in the two SDSS samples, it suggests that the reddening sources in these objects likely exist at larger radial distances than the narrow line regions from the central nucleus.

*Subject headings:* quasars: absorption lines, galaxies: evolution

## 1. Introduction

Mass outflows in quasars, seen as blueshifted broad absorption lines (BALs), have recently become a plausible explanation for quasar feedback (e.g., Faucher-Giguère et al. 2012). Feedback has been invoked to explain several phenomena such as the  $M-\sigma$  relationship for supermassive black holes (SMBH) and their host galaxies (e.g., Silk & Rees 1998; Di Matteo et al. 2005) as well as the quenching of star formation in the host galaxy (e.g., Hopkins et al. 2013; Dubois et al. 2013). The recent advancement is due in large part to studies of a subclass of BAL quasars that exhibit absorption troughs from both resonance and metastable state lines of low ionization species, namely from Fe II and Fe II\* (i.e., FeLoBALs; Korista et al. 2008; Moe et al. 2009; Dunn et al. 2010; Bautista et al. 2010) and in one case from high ionization lines (S IV and S VI\*; Borguet et al. 2013). The combination of these lines with photoionization modeling yields the density and therefore the distance and energy output of the outflows. These observational results have led to recent work to explain the physical mechanisms behind the driving of the gas (e.g., Ostriker et al. 2010; Debuhr et al. 2010; Silk & Nusser 2010).

Unlike the more common high ionization BALs, which demonstrate strong absorption due to C IV and appear in approximately 20% of all quasars (Knigge et al. 2008; Hewett & Foltz 2003), low ionization absorption troughs due to species like Mg II (LoBALs) and Fe II (FeLoBALs) are relatively uncommon in optical spectral surveys (e.g., White et al. 2000; Hall et al. 2002; Silk & Nusser 2010). Furthermore, many LoBALs (Zhang et al. 2010) and FeLoBALs (Weymann et al. 1991; Sprayberry & Foltz 1992; Reichard et al. 2003; Urrutia et al. 2008) display signs of large color excess due to dust extinction. The extinction commonly observed in these objects appears to be best described by a Small Magellanic Cloud (SMC) extinction curve (Richards et al. 2003; Hopkins et al. 2004). The combination of rarity and reddening properties of these objects has led studies to postulate

about their relevance in quasar evolution. One plausible scenario is that FeLoBALs are normal BAL quasars with a specialized sight-line that grazes the edge of the putative dusty torus (see Hall et al. 2002). This simultaneously explains the strong reddening present in many objects and provides a source of opacity that decreases the ionizing flux impinging on the outflowing gas allowing for clouds to form singly ionized species (see Dunn et al. 2010 and references therein). An alternative scenario suggests that FeLoBALs represent an evolutionary state during a quasars lifetime (Egami et al. 1996; Becker et al. 1997; Hopkins et al. 2008; Urrutia et al. 2008; Glikman et al. 2012) where the quasar sheds its obscuring dust and gas. The dust source during this process could provide reddening at any distance from the nucleus.

While recent studies of FeLoBALs have determined distances for these outflows, the radial location of the dust source is unknown. This was especially relevant in the object QSO0318–0600, where we accurately determined the density of the outflowing gas due to the presence of troughs from metastable, excited-state lines (Fe II, Si II, and Ni II). Combining the density with photoionization modeling yielded a radial distance of several kiloparsecs from the nucleus for the outflowing material. Other studies have shown that large distances such as this appear in several FeLoBAL objects (e.g., SDSS J0838+2955; Moe et al. 2009). Like many FeLoBALs, QSO0318–0600 is an extremely reddened quasar (see discussion in Dunn et al. 2010), where the impact of the dust on the full spectral energy distribution (SED) is significant. Thus, should the dust source be located between the outflow and the nucleus (similar to the torus scenario) then the ionizing flux reaching the outflowing gas would be severely diminished. This uncertainty in dust location affects the distance determination and in turn the determined energy output by up to a factor of 4.

We take the first steps to ascertain the radial location of dust in a sample of FeLoBALs, which has implications for the generation of low ionization species. We begin by discussing

the method for spectral analysis in §2 and determine the respective sample for this method in §3. In §4, we determine and compare the continuum and emission line reddenings for the objects, which provides the radial locations of the dust sources. Finally, we summarize the findings and discuss the implications in §5.

## 2. Diagnostic Tool to Determine Radial Location

As mentioned earlier, the sources of dust in LoBAL and FeLoBAL quasars could exist in two different radial distance regimes, either interior or exterior to the outflowing gas with respect to the nucleus. To explain the commonly observed reddening in FeLoBALs, we assert logically plausible sources for the dust. For example, given the unified model of active galactic nuclei (AGN, Antonucci & Miller 1985; Urry & Padovani 1995), a grazing sightline past the edge of the torus in the vicinity of the AGN provides the observed reddening, which we refer to as scenario 1. The dust torus would provide the simplest simultaneous explanation for the reddening and the necessary decrease in ionizing flux required to generate low ionization species in these types of outflows. Other structures do exist such as nuclear dust spirals observed in spatially resolved low- $z$  quasars and Seyfert galaxies that could potentially provide a reddening near the nucleus. In scenario 2, a source not necessarily associated with the AGN such as a galactic dust lane at kpc scale distances is the cause of the reddening. Without spatially resolved imaging of the host galaxy we cannot distinguish which specific structure is present, but we are able to determine whether the dust source lies close to the nucleus or at galactic distances.

Observationally, the torus in scenario 1 would redden both the continuum source and the broad emission lines (BELs) that arise from the broad line region (BLR) close to the accretion disk-SMBH system. By comparison, the narrow emission lines (NELs), which are generated in the narrow line region (NLR) at a much larger distance (100s of parsecs in

typical quasars; Peterson 1997), would remain unextincted much like the work on Seyfert 1.8 and 1.9 galaxies by (Trippe et al. 2010) and on the Seyfert 1 galaxy MCG–6–30–15 by (Reynolds et al. 1997)). In the second scenario, a large structure at a galactic scale would redden the continuum, BLR, and NLR by approximately similar amounts. Furthermore, a structure at kpc scale distances would be statistically unlikely to cover only one of the two AGN components. Thus, direct comparison of the continuum and NLR reddening demonstrates whether the reddening occurs interior (scenario 1) or exterior (scenario 2) to the NLR. A similarly reddened NLR compared to the continuum (i.e.,  $E(B-V)_{NLR} \approx E(B-V)_{cont}$ ) suggests that the dust lies exterior to the NLR and cannot be explained by a dust torus. A reddening value of the continuum significantly larger than that of the NLR implies that the dust is in the vicinity of the AGN and is likely associated with the dust torus.

It is important to note that the BELs should be as reddened as the continuum in either scenario, as the BLR lies interior to the torus. Ideally we would use the emission ratios of the Balmer BELs in conjunction with the NELs to determine if scenario 1 applies. However, it has been shown that BEL line ratios in AGN are not well described by case-B recombination in some objects (e.g. Kwan & Krolik 1981; Korista & Goad 2004). This primarily stems from high densities associated with the BLR region, which leads to radiative transfer and collisional effects that impact the description of recombination present in the gas. Because measurements of the Balmer decrement of BELs are potentially poor approximations of the extinction, we only compare the extinctions of the continuum source and the NEL.

Unlike the BELs, the NELs are adequately described by case-B recombination as the number density is significantly lower ( $10^4 \text{ cm}^{-3} < n_H < 10^6 \text{ cm}^{-3}$ ), which implies that the case-B approximation is valid (Osterbrock & Ferland 2006). Furthermore, the ratio of  $H\alpha$

to  $H\beta$  only spans the range 2.74–2.86 (due to density) at temperatures of approximately 10,000K, implying that the ratio is relatively insensitive to temperature differences.

Assuming case-B, the reddening is defined as:

$$E(B - V) = \frac{2.21}{R_{H\alpha} - R_{H\beta}} \log \frac{2.76}{\frac{f_{H\alpha}}{f_{H\beta}}}, \quad (1)$$

where  $R_{H\alpha}$  and  $R_{H\beta}$  are the values of the SMC reddening curve at  $H\alpha$  and  $H\beta$ , respectively, and  $f_{H\alpha}$  and  $f_{H\beta}$  are the peak fluxes of the emission lines. We use 2.76 as the intrinsic Balmer ratio as determined by case-B recombination (Osterbrock & Ferland 2006). While  $H\alpha$  and  $H\beta$  are the optimal lines for this process, in the majority of our sample we are only able to observe  $H\beta$  and  $H\gamma$  due to the combination of redshift and spectral range of the Sloan Digital Sky Survey (see §3). Thus, we also use the ratio of  $H\gamma$  to  $H\beta$  (0.474, Osterbrock & Ferland 2006), which likewise spans a relatively narrow range of 0.469–0.476 for case-B recombination.

### 3. Survey

#### 3.1. Sample Selection

To employ the method outlined in Section 2, we require a sample of quasars that demonstrate FeLoBAL troughs as well as strong narrow line Balmer emission. To obtain the largest number of objects, we utilize the Sloan Digital Sky Survey (SDSS) spectroscopically observed quasars (Richards et. al 2009) through Data Release 7 (DR7, Schneider et al. 2010). Quasar spectra in the SDSS-III catalog are unusable for this study as the spectra in that catalog are not accurately flux calibrated (Dawson et al. 2013). We access and download the calibrated spectra through the online Catalog Archive Server (CAS).

We limit our search primarily by redshift. A redshift of  $z=0.45$  is sufficient to redshift

the Mg II ( $\lambda\lambda 2796, 2804$ ) emission line into the spectral range of SDSS (approximately 3800 to 9200 Å) and permit absorption trough detections for Mg II up to approximately 10,000 km s<sup>-1</sup>. A redshift of 0.45 places the Balmer H $\alpha$  ( $\lambda 6563$ ) at  $\approx 9500$  Å and out of the spectral range of SDSS, thus precluding simultaneous observation of BAL troughs and the H $\alpha$  emission line. We select an upper limit on the redshift determined by the Balmer H $\beta$  ( $\lambda 4861$ ) line, which redshifts out of the spectral range at approximately  $z=0.90$ . We further limit the sample by magnitude as objects fainter than r magnitude of 19 will have substantial noise that can potentially obscure weaker narrow Balmer emission lines. The resulting sample contains 8,511 quasars.

Next, we plot and visually inspect these spectra for blueshifted Mg II and Fe II BALs. To reduce the search time we examine spectra for Fe II troughs in those objects that contain Mg II BALs; previously these troughs have only been observed in objects that show Mg II absorption, which is typically easier to identify. We define BALs here to be any intrinsic absorption troughs in the quasars spectrum (i.e., outflowing gas ejected by the AGN, see Barlow & Sargent 1997). Zhang et al. (2009) suggested that a velocity width of 1600 km s<sup>-1</sup> simultaneously maximizes the frequency of which BALs are intrinsic outflows and also maximizes completeness of a BAL sample. To this end, we only include objects with contiguous trough widths greater than 2,000 km s<sup>-1</sup>. A width of 2,000 km s<sup>-1</sup> is similar to the Absorption Index (*AI*) method used in Trump et al. (2006) and Hall et al. (2002). A width of 2,000 km s<sup>-1</sup> is also sufficient to blend the two members of the Mg II doublet and facilitate visual inspection. This provides a conservative lower limit on objects with intrinsic absorption. Comparing to the Zhang et al. determinations, our sample is complete to slightly less than 75%, but over 90% of the objects are bona fide outflows tied to the quasar. Quasars in the lower redshift ranges only provide minimal velocity coverage of the UV 3 Fe II multiplet ( $\approx \lambda 2600$ ). For the redshift range of 0.45–0.50, we detect only those BALs at low velocity ( $v \sim 6000$  km s<sup>-1</sup> at  $z=0.50$ ) and obtain only a lower limit on the



number of objects with Fe II BAL troughs.

The last criterion we impose on the sample is to select objects with Mg II and Fe II BALs that show narrow emission lines due to  $H\beta$  and/or  $H\gamma$  ( $\lambda 4341$ ) in conjunction with [O III]  $\lambda 5007$  emission. We characterize this as a distinct emission feature that has a maximum FWHM less than  $1000 \text{ km s}^{-1}$ . This value is consistent with the findings of Richards et al. 2003 for [O II]  $\lambda 3727$  and [O III] emission lines in reddened quasars. The peak intensity must be distinguishable from the BEL (i.e., at least  $3 \sigma$  above the noise level at the BEL peak).

### 3.2. Survey Objects and Properties

In our sample, we find 70 quasars (approximately 0.8% of the full 8,511 quasar sample) that show Mg II troughs matching the criteria established in the previous section. This is similar to other spectroscopically selected samples in the optical (e.g., approximately 1.3% via the *AI* method in Trump et al. 2006). Of these 70 objects, 15 showed BALs attributed to Fe II (0.2%). To determine the presence of Fe II troughs, we check for radial velocity agreement with Mg II as demonstrated in Figure 1 for a high resolution spectrum of SDSS J0149–1016. Finally, only 4 of the 15 objects also demonstrate evidence of strong narrow emission due to hydrogen, [O III], and [O II]. Figure 2 displays the SDSS spectra of these 4 objects (and 1 additional object explained below). The Mg II and Fe II BAL troughs are evident in these spectra. Furthermore, in all 4 cases, we find evidence of troughs due to excited, metastable state lines of Fe II. We list the SDSS identifiers,  $r'$  magnitudes, and redshifts for all 70 of the BAL quasars in Table 1 and indicate which objects in the sample show troughs due to Fe II and strong narrow  $H\beta$  emission. Of the 4 FeLoBALs with detectable  $H\beta$  emission, only SDSS J 0802+5513 also has a detectable  $H\gamma$  narrow emission line.

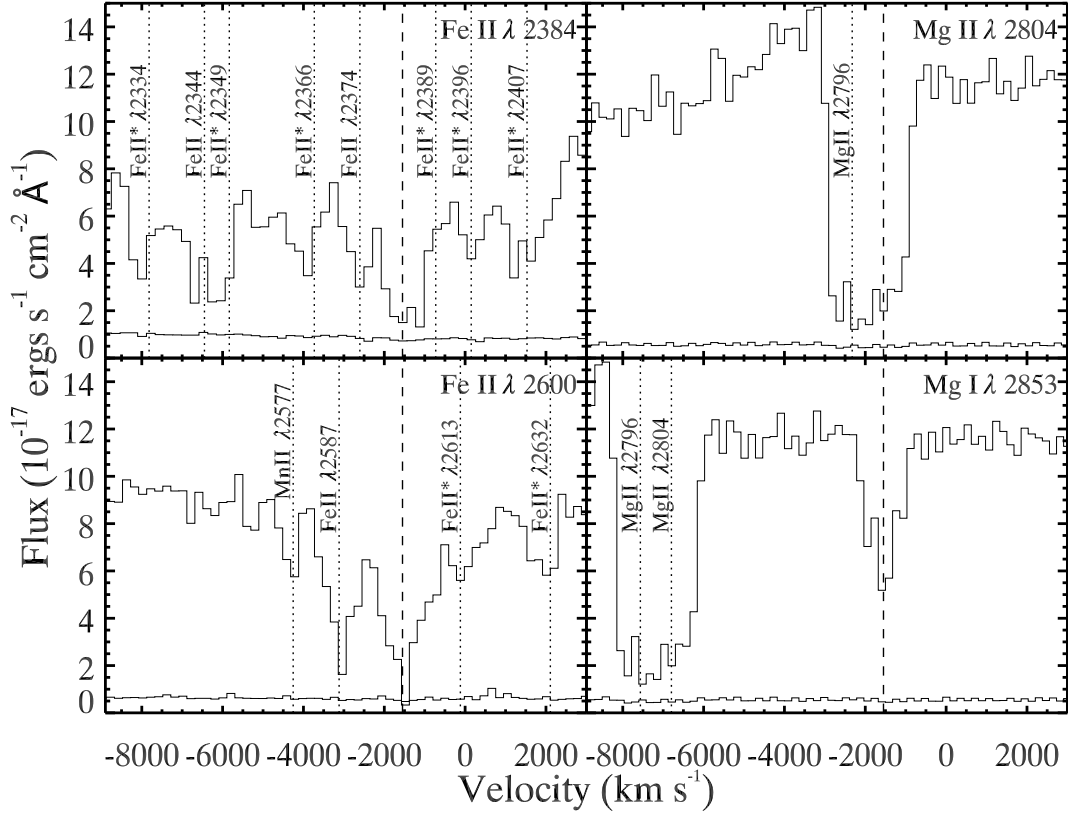


Fig. 1.— Absorption trough identifications for Mg I, Mg II, Mn II and several resonance and excited state (noted with an asterisk) Fe II lines in the SDSS spectrum of SDSS J0802+5513. The primary absorption trough, marked with a dashed line, occurs at approximately  $-1600 \text{ km s}^{-1}$ . Each panel is plotted in velocity from the respective ions listed in the upper right. Other notable lines are indicated with dotted lines at shifts of  $1600 \text{ km s}^{-1}$  from their respective rest wavelengths.

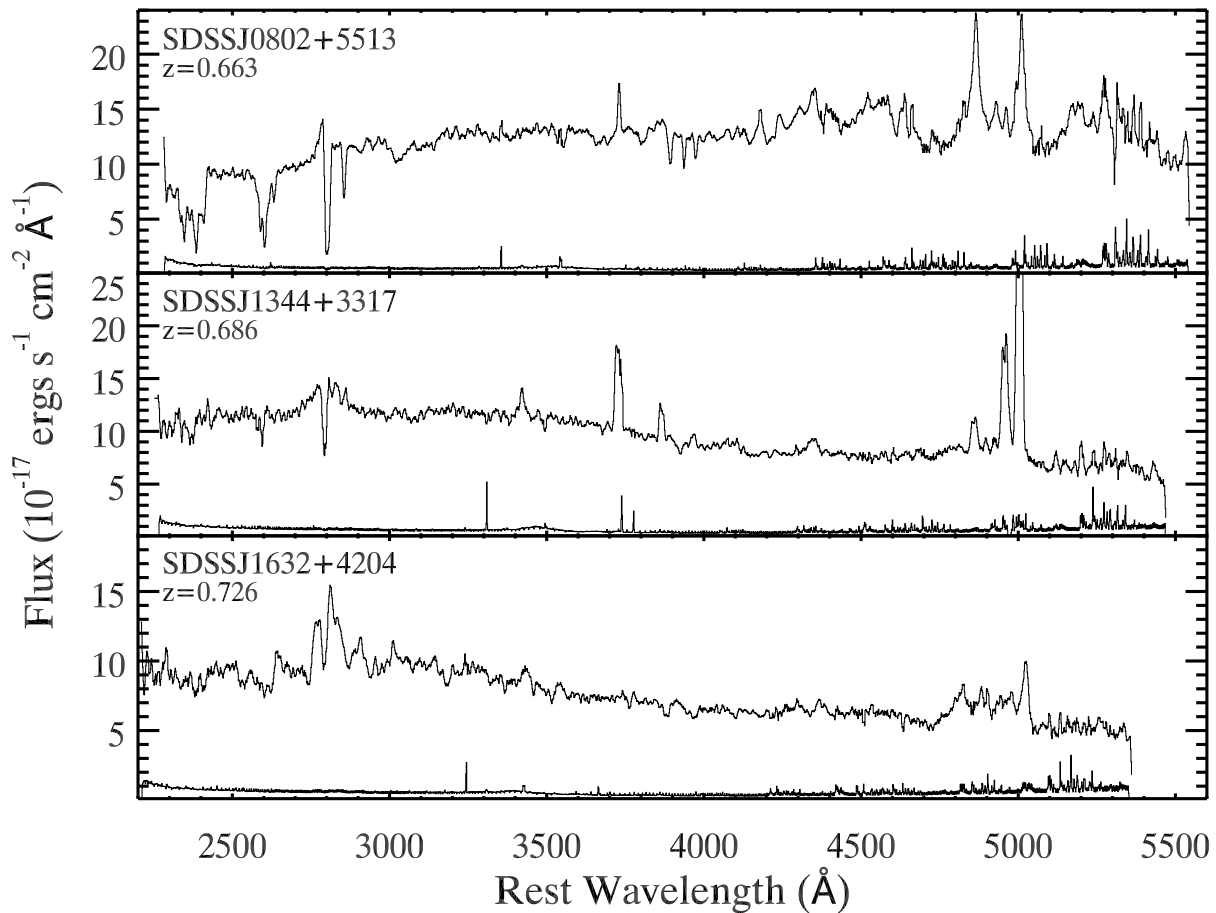


Fig. 2.— Spectra, plotted in the rest frame, for objects demonstrating BALs due to MgII, with troughs due to FeII, and strong NELs ([O III] and H $\beta$ ). The object SDSS names and SDSS measured redshifts are listed in the upper left of each panel. The first 4 spectra were taken by SDSS, while the final spectrum (SDSS J0149–1016) was taken with the Magellan MIKE spectrograph. The flux uncertainties are plotted beneath each spectrum with black histograms.

We also include in our study the object SDSS J0149–1016 (R.A. 01:49:06.736, decl. -10:16:49.27). While this object has a redshift of 0.364 and is therefore not included in our search statistics, we have a Magellan Inamori Kyocera Echelle (MIKE) spectrum of this quasar (also shown in Figure 2). MIKE is a high throughput double echelle spectrograph (for details see Bernstein et al. 2003). The spectrum was taken on Sept. 15, 2006 and has been reduced with the standard MIKE Interactive Data Language (IDL) reduction tools. The continuum flux levels agree with the SDSS spectral observation (Sept. 22, 2001). SDSS J0149–1016 was observed with a high resolution spectrograph with the intent of determining the outflow’s radial distance. This work is still in progress. In the meantime, this spectrum provides an excellent opportunity to compare the reddening determinations from the combinations of  $H\alpha$ ,  $H\beta$ , and  $H\gamma$  NELs with the continuum as the MIKE spectrum has a larger spectral range ( $\sim 3600\text{--}9300 \text{ \AA}$ ) than SDSS that provides coverage of the Balmer series as well as the Mg II BAL and Fe II absorption troughs (see Figure 1).

To strengthen the continuum reddening determinations in §4, we complement the SDSS spectra with data from the 2 Micron All Sky Survey (2MASS; Skrutskie et al. 1997). These IR data provide a longer baseline for the reddening determinations. We use a matching radius of  $3''$  and obtain the J, H, and K magnitudes for each object. We list the 2MASS magnitudes for the sample in Table 1. The uncertainties for 2MASS data are typically 0.10–0.15 magnitudes.

## 4. Reddening Determinations

### 4.1. Continuum Reddening

We use the SDSS spectra to determine the continuum reddening rather than SDSS photometry because the combination of varying BEL emission line fluxes, and more

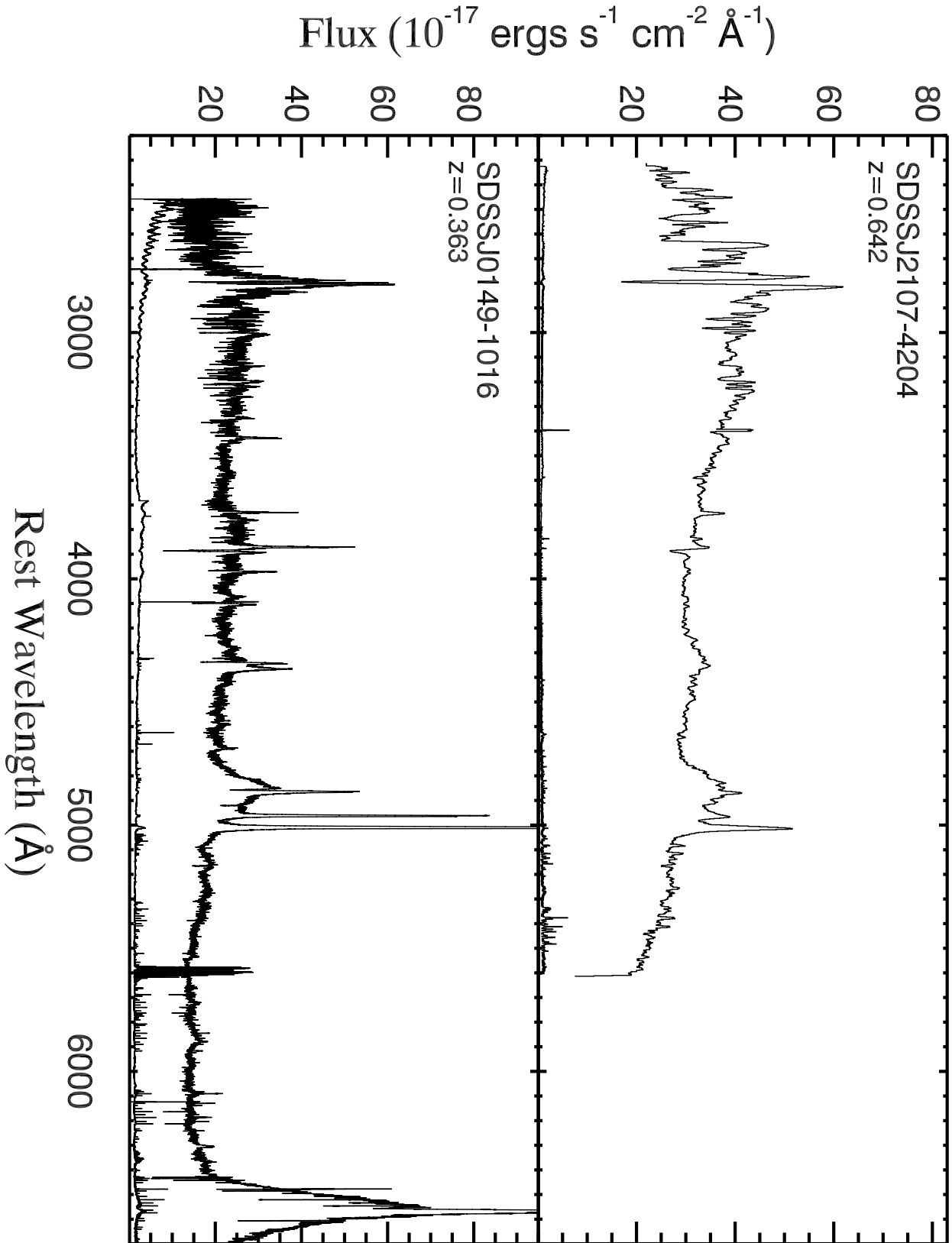


Fig. 2b. - Cont.

importantly, the presence of BALs can significantly impact the  $E(B-V)$  determinations. We begin by correcting for Milky Way extinction ( $E(B-V)_{MW}$ ) as determined by the online extinction calculator at the NASA/IPAC Extragalactic Database (Schlafly & Finkbeiner 2011). Next, we correct for the intrinsic reddening of the object ( $E(B-V)_Q$ ) in the restframe of the quasar using an SMC extinction curve (see Section 1; Richard et al. 2003; Hopkins et al. 2004). Because the SMC curve may not provide the most accurate description of the reddening at short wavelengths (i.e., in the far UV regime; see Dunn et al. 2010), we fit the restframe spectrum in the near UV and visible regimes, which are less dependent on the dust grain size distribution. To represent a typical unreddened quasar spectrum, we use the SDSS composite spectrum (Vanden Berk et al. 2001). With regards to the intrinsic shape of the full spectral energy distribution (SED), Vanden Berk et al. (2001) and Richards et al. (2003) found that the distribution of quasar SED shapes from SDSS data is Gaussian with a relatively small spread ( $\sigma = 0.30$ ). In addition, Hopkins et al. (2004) showed that large reddening ( $E(B-V) > 0.1$ ) occurred in less than 1% of their sample of SDSS objects, in agreement with other surveys such as Urrutia et al. (2009) and Glikman et al. (2012). Thus, any large deviation from the composite SDSS spectrum is likely due to dust extinction.

We de-redden each LoBAL spectrum in the sample by the SMC curve to match the continuum levels of the SDSS composite spectrum. We complement the SDSS spectrum with 2MASS photometry, when available, which provides data over a larger wavelength baseline that are less affected by reddening for the fit. The best fit is determined by matching regions of continuum between the two spectra shortward of approximately 5000 Å. Due to the differences in the intrinsic continuum slope, presence of emission lines, and various depths and velocities of the BALs, we determine fits via visual inspection. While these fits are subject to the possibility of host galaxy contamination in the quasars' spectra, a lack of strong stellar absorption troughs in the restframes of the quasars suggests that the host galaxy contributions are relatively small. We derive limits on uncertainty from

under and over compensating for the reddening given the limits of the spectral noise in the LoBAL’s spectrum. We also model the general shape of the continuum to provide predictions of flux levels in the infrared range with both a Mathews & Ferland (1987) SED and the “UV-soft” SED of Dunn et al. (2010) and find little difference in the fits between the two SEDs across the observed range. We show examples of the FeLoBAL fits in Figure 3 and list the  $E(B-V)_{MW}$  values, determined quasar extinction values ( $E(B-V)_Q$ ), and uncertainties for the LoBALs in Table 2. Regarding SDSS J0149–1016, because we have the Magellan MIKE and SDSS spectra we measure the continuum reddening for both. We list the SDSS measured value ( $0.10 \pm 0.02$ ) in Table 2 and find a consistent value from the Magellan spectrum of  $0.11 \pm 0.03$ .

As stated in Section 2, the AGN SED slopes likely have a Gaussian distribution centered around the slope of the average spectrum. This implies, especially in a sample of non-BAL objects, that a fraction of the objects will have bluer slopes than the SDSS composite spectrum. We observe this in a small, randomly selected subset of non-BAL quasars using our fitting technique as a negative  $E(B-V)_Q$ , which suggests that these objects have little or no reddening. Similar to the non-BAL quasars, we only find a few objects in the LoBAL sample with appreciable negative  $E(B-V)_Q$  values. We summarize the relative percentages of LoBALs in several reddening ranges in Table 3. Approximately 49% of the LoBALs in the sample have an  $E(B-V)_Q$  consistent with zero and 23% of the objects have significant reddening ( $E(B-V)_Q \geq 0.1$ ). This is a substantially larger fraction compared to a general sample of non-BAL quasars (1% in the same range; Hopkins et al. 2004) and is consistent with the SDSS Data Release 5 sample of Mg II LoBALs measured by Zhang et al. (2010).

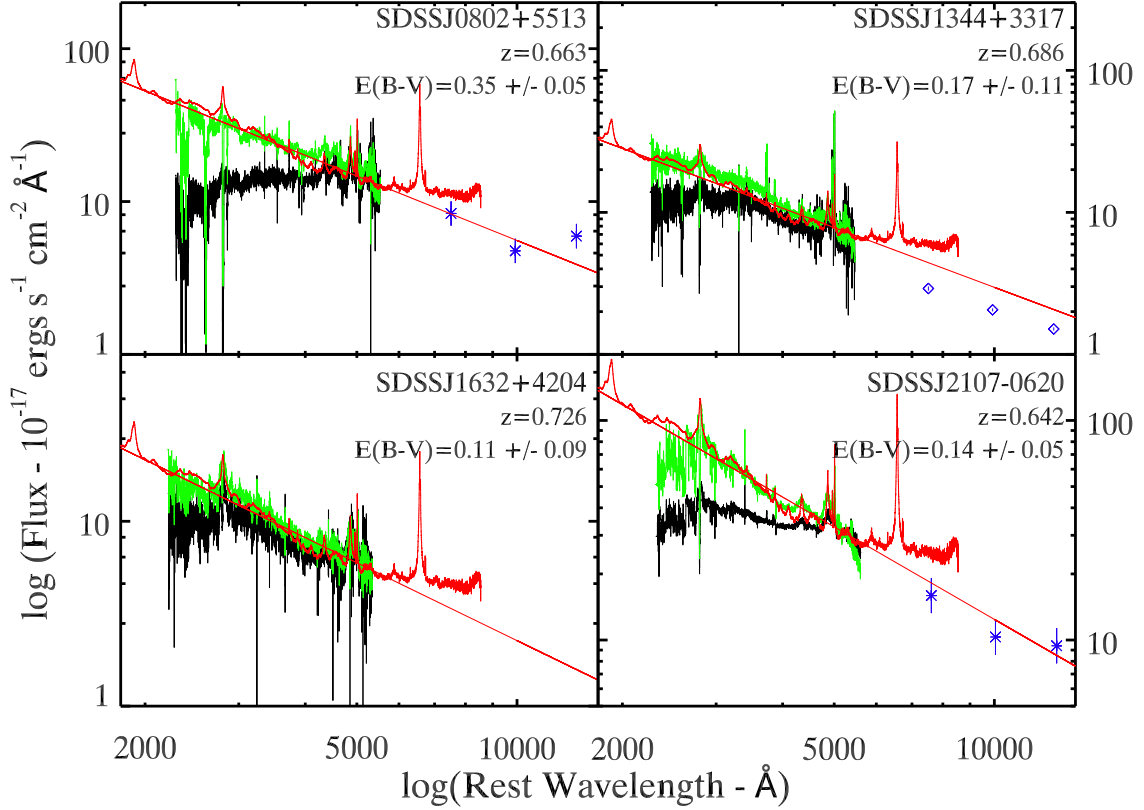


Fig. 3.— Spectral correction for both Milky Way and host galaxy reddening for the FeLoBAL objects in the SDSS survey. The black histogram is the SDSS spectrum, the red histogram is the SDSS composite spectrum, the red curve is the “UV-soft” SED adjusted to the SDSS flux at 5100 Å, the green histogram is the dereddened spectrum, and the blue asterisks and diamonds are the flux values and uncertainties derived from the 2MASS and UKIDSS photometry, respectively. The SDSS composite spectrum likely deviates from the SED (and the 2MASS data) longward of 5000 Å due to host galaxy contamination in the composite spectrum (Vanden Berk et al. 2001). The derived values of  $E(B-V)$  are listed along with the redshift of each object in the upper right. Note that the data near 4500 Å for SDSS J0802+5513 are poor matches to the SDSS spectrum, primarily due to strong Fe II emission (similar to EV1 of Boroson & Green 1992). The poor fit to the UKIDSS data for SDSS J1344+3317 is plausibly due to a 10% decrease in flux of the object in the time span between the observations (approx. 2 years) given the similar slopes.



## 4.2. NLR Reddening

To determine the reddening of the hydrogen NELs, we first normalize the continuum and the BEL (as we do not require any physical information from the BLR, see §2) with a spline fit and subtract the fit to isolate the NEL. Using the [O III]  $\lambda$ 5007 emission line as a template for the NEL, we scale the template to match the normalized hydrogen NELs (as demonstrated in Figure 4 for SDSS J0802+5513). We use this template primarily to determine the portion of the total emission profile that is due to the NEL and to also account for any asymmetries in the line profile commonly found in NELs such as multiple peaks (e.g., SDSS J1344+3317) and asymmetric blue wings (Heckman et al. 1981; Greene & Ho 2005; Komossa et al. 2008). We do not model the lines with Gaussian fits, which would require several fits that do not yield any physical information. To determine the measurement uncertainties, we add the average flux uncertainty percentage across the peak of the line with the continuum determination uncertainty (approximately 3%). These are listed in Table 2.

For SDSS J0149–1016 (also shown in Figure 4), there are three important features. First, we fit  $H\alpha$ ,  $H\beta$ , and  $H\gamma$  due to the broader spectral coverage. Second, this object also shows structure in the narrow emission lines, seen in both the [O III] doublet  $\lambda\lambda$ 4959, 5007 and Balmer series. Finally, this object shows blueshifted Balmer absorption troughs, which implies a high density for the outflowing gas (see §5 for further discussion of the physical implications). In the measurements of the emission features, the absorption troughs are important as they directly impact the blue emission wing for fitting. Therefore, our matches are primarily compared to the red wings and peaks of the emission lines.

In the case of SDSS J1632+4204, we are unable to generate an adequate template for the NEL. The [O III] doublet ( $\lambda\lambda$ 4959, 5007) lies in the telluric absorption corrected region

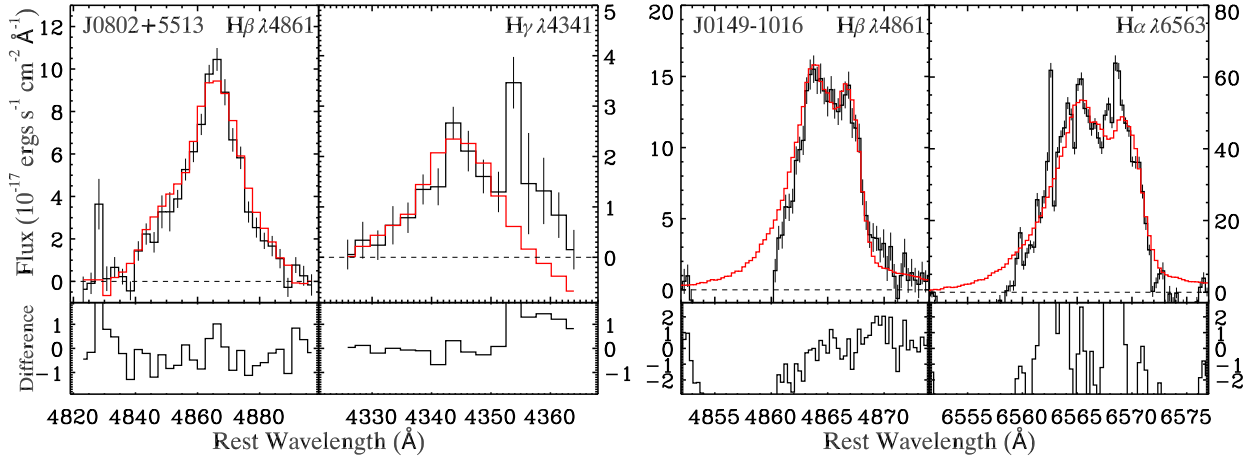


Fig. 4.— **Left:** Plots of the H $\beta$   $\lambda$ 4861 and H $\gamma$   $\lambda$ 4341 narrow emission lines with their fits for SDSS J0802+5513. The black histograms are the hydrogen emission (after subtracting the broad emission lines) and the red histograms are templates created from the [O III] emission line ( $\lambda$ 5007) scaled to fit the hydrogen lines. The [O III] lines are boxcar smoothed by 5 pixels, which effectively removes problematic pixels due to telluric line subtraction and maintains the general shape of the [O III] line (FWHM =  $800 \pm 100$  km/s). The poor fit to the H $\gamma$  red wing is presumably due to contamination by [O III]  $\lambda$ 4363. Thus, we fit the blue wing and peak. Residual differences are plotted in the lower sections. We determine uncertainties in fitting by taking the difference of matching the peaks to matching the emission line wings, which are comparable to the average of the residual differences (better than 20% across several pixels). **Right:** Plot of the H $\alpha$  and H $\beta$  emission lines in SDSS J0149–1016. The data is rebinned by a factor of two and yields a ratio of 3.23 between H $\alpha$  and H $\beta$ . The data points blueward of the emission peak reflect the BALs seen in the Balmer series. The largest differences are due to spurious points in the data, which are from imperfect telluric corrections.

of the spectrum, which provides significant errors in an [O III] template as well as any measurement of the H $\beta$  emission. There is also no indication of a strong [O II]  $\lambda$ 3727 line to provide a template. Due to the absence of an uncontaminated line for the template but clear presence of H $\beta$  emission, we include this object in the survey statistics, but cannot fit the H $\beta$  line.

As previously identified in Section 3, the only object in the SDSS survey that exhibits a measurable narrow emission line from H $\gamma$  is SDSS J0802+5513. To determine the NLR reddening values in the remaining two objects with measurable H $\beta$  emission lines, we use the template to determine the upper limit of H $\gamma$  emission based on the statistical error of the data (similar to the method used in Dunn et al. 2010 for determining absorption trough limits). We compare a scaled emission line template to the continuum region where the line

would be detected. We maximize the scale to match the amount of noise present in the spectral region, which provides the largest possible amount of emission present from  $H\gamma$ . We show this for SDSS J1344+3317 and SDSS J2107–0620 in Figure 5. Both objects show some signs of a weak and noisy  $H\gamma$  line, but we conservatively list these measurements as limits. Finally, we list the  $E(B-V)_{NLR}$  determinations and limits for these two objects in Table 2 for each object in the sample.

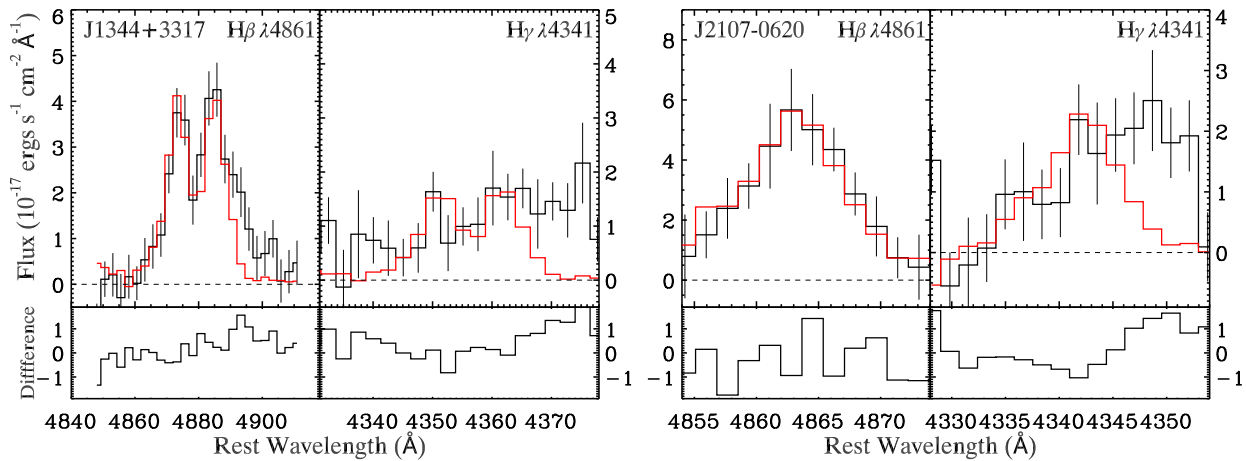


Fig. 5.— **Left:** Similar plot to Figure 4, however for SDSS J1344+3317. The fit to the  $H\gamma$  emission, is a firm upper limit determined by the flux uncertainties. As with Figure 4, the excess emission near 4370 Å is likely due to  $[O\text{III}]\lambda 4363$ . No boxcar smoothing was applied to the  $[O\text{III}]$  template for this object, as the emission lines in this object are free of telluric contamination. **Right:** Plot for SDSS J2107–0620. Unlike with SDSS J1344+3317, we boxcar smooth the oxygen line profile by a factor of 3 as the line is much noisier in this object’s spectrum. Also peculiar in this spectrum, the oxygen line appears to be shifted by approximately 2 Å from the Balmer lines, but does not affect the overall determined ratio.

While the major focus of this study pertains to FeLoBALs due to the recent distance determinations for the outflows of this type and the problems associated with reddening, we have also measured the NEL reddening for the regular LoBALs using the techniques listed above for the FeLoBALs. We list the values of  $E(B-V)_{NLR}$  for the LoBALs in Table 2.

### 4.3. Reddening Comparisons

Many studies of NEL/BEL/continuum reddening in AGN (e.g., Reynolds et al. 1997) compare hydrogen column densities ( $N_H$ ) between components of the unified model. However, Maiolino et al. (2001) showed that the  $E(B-V)/N_H$  ratio ranges by two orders of magnitude depending on the type of dust in the object. It has also been shown (Dunn et al. 2010; Hall et al. 2004) that while the reddening curves in many AGN are best fit by an SMC curve, in extreme cases of reddening the continuum is not well fit at short wavelengths. This disparity potentially affects any dust column density determinations. Thus, we directly compare  $E(B-V)$  values between the AGN components.

Comparing the values for the FeLoBALs in Table 2, we find that three objects show clear evidence of reddening in both the continuum and the NELs (SDSS J0802+5513, SDSS J1344+3317, and SDSS J2107–0620). While SDSS J0149–1016 shows measurable continuum reddening, due to the uncertainties in the line fitting, the ratios and the resulting  $E(B-V)_{NEL}$  values are consistent with either reddening scenario. As stated previously, the NELs in SDSS J1632+4204 cannot be measured, but the object does show an appreciable continuum reddening.

All three FeLoBALs with measurable  $H\beta$  NELs listed above, demonstrate a dusty source that simultaneously reddens both the NLR and the continuum. This implies that the dust must exist radially exterior to the NLR and precludes a torus reddening source for these three FeLoBALs. Due to the relatively low number of available objects and the combination of low continuum reddening ( $E(B-V)_Q \approx 0.1$ ) with large uncertainties in SDSS J0149–1016, we cannot state conclusively if FeLoBALs in general share this physical picture. It is notable, though, that all three objects with significant continuum reddening appear to have reddening sources farther from the central black hole than the NLR.

For the regular LoBALs, the majority of the LoBALs have  $E(B-V)_Q$  values consistent

with no reddening; we find that the majority of the  $E(B-V)_{NLR}$  values are likewise small. There are 6 LoBALs of the 70 in the survey with  $E(B-V)_Q > 0.1$ . Of these 6 objects, three have measurable  $H\beta$  lines: SDSS J1010+1843, SDSS J1700+3955, and SDSS J1703+3839. We find an  $E(B-V)_Q=0.11\pm0.03$  for SDSS J1010+1843. The emission line measurements yield a similar value though with a significant uncertainty. SDSS J1700+3955 has moderate continuum reddening with a relatively large uncertainty ( $E(B-V)_Q=0.16\pm0.14$ ). The measured NLR reddening is consistent with the continuum within the large uncertainties of the two values ( $E(B-V)_Q=0.59\pm0.30$ ). Finally, SDSS J1703+3839 has a large reddening value of  $E(B-V)_Q=0.40\pm0.03$ , but unfortunately has no measurable  $H\gamma$  emission line. The limit derived from  $H\gamma$  yields an  $E(B-V)_{NLR} > 0.2$  and is certainly in line with the continuum determination. Similar to the FeLoBALs, the LoBALs in the survey also have continuum and NLR reddenings that are similar within the uncertainties, which tentatively suggests that the reddening sources in LoBALs exist at larger distances than their NLRs.

To illustrate the relationship, we plot in Figure 6 the continuum reddening against the NLR reddening for both the LoBAL and FeLoBAL quasars in the entire sample. The plot shows a significant agreement between the two reddenings determinations for both populations of quasars. This nearly 1-to-1 relationship supports scenario 2 for the physical picture for the quasars in this sample.

## 5. Summary and Conclusions

We have assembled a subsample of 70 LoBAL quasars from a sample of 8,511 quasars with redshifts between  $0.45 \leq z \leq 0.80$  from the SDSS. Of the 70 quasars, 23 have detectable narrow emission lines from  $H\beta$ . This sample also contains 15 FeLoBAL quasars, 4 of which show signs of narrow Balmer emission lines. Therefore, narrow Balmer emission only appears to arise in approximately 27% of FeLoBAL quasars. Both the LoBAL sample and

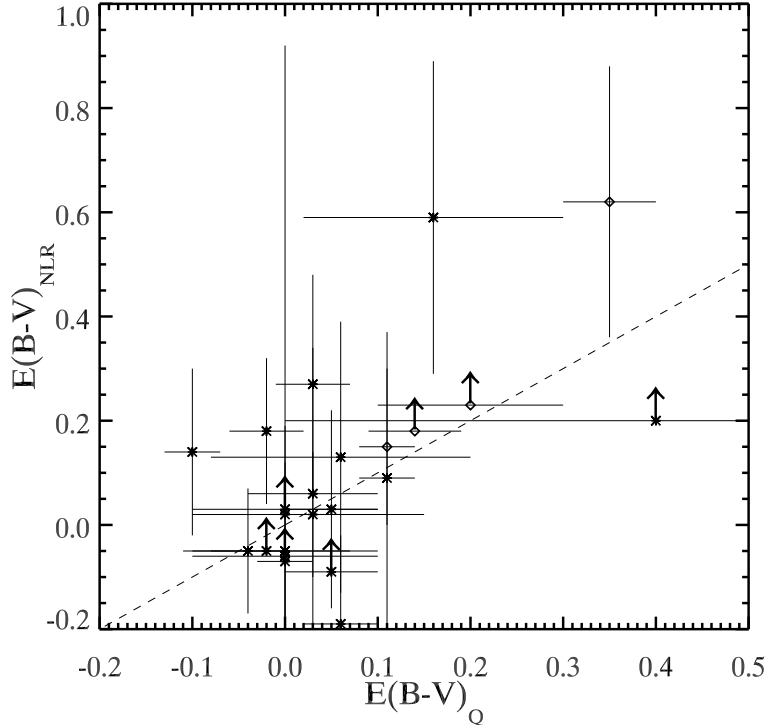


Fig. 6.— Comparison of the reddening for the quasar’s continuum (horizontal axis) and the reddening of the NLR (vertical axis). Diamonds represent the FeLoBALs, while x’s represent LoBALs. Vertical arrows illustrate objects with a lower limit determination for the NLR reddening.

FeLoBAL subsample clearly have a large fraction of objects with significant continuum reddening ( $\sim 23\%$  with  $E(B-V)_Q \geq 0.1$  for Mg II BALs and 4 Fe II objects or  $\sim 23\%$  with  $E(B-V)_Q \geq 0.1$ ).

From measurements of the reddening of the continuum and narrow line region, we find that three FeLoBAL quasars (out of 5 total objects, 4 from our sample and one additional quasar with a Magellan MIKE spectrum) have reddening sources that must exist radially exterior to the NLR from the AGN and are not directly tied to the dust torus. Due to telluric contamination, the  $H\beta$  Balmer emission in one object (SDSS J1632+4204) cannot be measured. Although the final object shows NLR reddening that is consistent with a radially exterior source, due to relatively low reddening ( $E(B-V)_Q \approx 0.1$ ) and significant

uncertainties in the emission line fits, we cannot conclusively state which physical picture applies. Also, as strong NELs do not appear to be ubiquitous to FeLoBALs, these objects could potentially be inherently different from the general population.

Given that every measurable object in the FeLoBAL sample has a similar physical picture, the findings hint that the reddening frequently observed in FeLoBALs is due to a source situated outside of the outflow from the AGN. In studies of FeLoBALs, (e.g., Moe et al. 2009; Dunn et al. 2010; Borguet et al. 2013) the outflow distance determinations have all yielded distances of several kpc. Because the objects in our FeLoBAL survey all suggest that the dust is located radially exterior to the outflow, the dust would likewise exist at kpc scale distances (assuming these objects are similar to previously studied FeLoBALs). A simple explanation for a host of the dust would be the outflows themselves. This could be further evidence that FeLoBAL quasars are evolutionary states of disrupted systems associated with major galaxy mergers as suggested by Glikman et al. (2012) and others.

In the case of SDSS J0149–1016, should the dust lie at a galactic scale, the implied outflow distance is likely significantly smaller than other measured FeLoBALs. This distance is implied by the presence of hydrogen Balmer line troughs, which are uncommon in BAL quasars. Hydrogen Balmer absorption typically suggests a rather large number density (albeit this depends on the ionization state of the gas). Thus, the dust would not arise due to the outflow but due to a source beyond the NLR such as a galactic dust lane or a nearby dwarf galaxy not associated with the outflow itself in at least this one object.

We have also examined the continuum and NLR reddening values in the larger sample of LoBAL quasars. While many of these objects have low continuum reddening values ( $(E(B-V))_Q < 0.1$ ), three objects exhibit relatively large reddening values. The two largest reddened objects both have Balmer emission lines that appear to have similarly large reddening; this suggests that like the FeLoBALs the dust exists at larger distances than the

NLR for LoBAL quasars.

Due to the rare nature of LoBAL and FeLoBAL quasars and the subsequent small sample size (especially with regards to the FeLoBAL quasars), the next step is to increase the number of targets. Obtaining spectra for higher redshift FeLoBALs observed by SDSS with higher resolution and larger wavelength coverage (similar to SDSS0149–1016) will increase the sample size and test these findings. Infrared spectra will provide coverage of the restframe optical regime for the stronger  $H\alpha$  and  $H\beta$  emission lines and yield a greater number of FeLoBALs with narrow Balmer emission suitable for the technique outlined in this study.

LCH acknowledges additional support from the Kavli Foundation, Peking University, the Chinese Academy of Sciences, and the Carnegie Institution for Science.



Table 1. SDSS Quasars with Mg II Outflows and Properties

SDSS Name	Plate-MJD-Fiber <sup>a</sup>	r' Mag	J Mag <sup>c</sup>	H Mag <sup>c</sup>	K Mag <sup>c</sup>	z <sup>b</sup>	Fe II <sup>d</sup>	H $\beta$ <sup>e</sup>
J010352.46+003739.7	51816-0396-471	17.42	16.157	15.425	14.074	0.703		
J024220.10-085332.7	51910-0456-291	18.86	-	-	-	0.799		y
J080248.19+551328.8	53384-1871-440	18.42	16.434	15.923	14.645	0.663	y	y
J080611.02+115029.0	53794-2418-616	18.88	-	-	-	0.616	y	
J080934.64+254837.9	52670-1205-588	17.93	17.029	16.469	16.099	0.545		y
J082231.53+231152.0	53317-1926-546	17.68	-	-	-	0.653		y
J083525.98+435211.3	52232-0762-175	17.55	16.407	15.961	15.131	0.568		
J085053.12+445122.4	52605-0897-359	17.41	16.222	15.967	14.909	0.542		
J085357.88+463350.6	52238-0764-248	18.22	16.758	15.892	15.287	0.549		
J092525.16+202139.0	53708-2289-183	18.51	17.067	16.080	15.288	0.460		
J093228.56+555344.8	51991-0556-251	18.76	16.611	15.820	14.826	0.876		
J093315.09+351944.2	52992-1594-348	18.87	-	-	-	0.525		y
J094225.42+565613.0	52253-0557-359	18.52	-	-	-	0.831		
J094443.13+062507.4	52710-0993-535	16.24	14.831	14.517	13.808	0.695		

Table 1—Continued

SDSS Name	Plate-MJD-Fiber <sup>a</sup>	r' Mag	J Mag <sup>c</sup>	H Mag <sup>c</sup>	K Mag <sup>c</sup>	z <sup>b</sup>	Fe II <sup>d</sup>	H $\beta$ <sup>e</sup>
J101038.76+184321.8	53768-2373-124	18.97	16.998	16.123	15.433	0.745		y
J101729.52+264146.7	53765-2350-435	18.70	-	-	-	0.526		y
J102802.33+592906.7	52316-0559-582	18.92	-	-	-	0.535		
J103036.93+312028.8	53440-1959-121	17.69	16.368	15.815	15.059	0.873		
J103255.37+083503.2	52734-1240-316	17.73	15.750	15.641	15.229	0.891	y	
J104122.84-005618.4	51913-0274-060	18.50	16.951	16.176	15.358	0.497		y
J104210.43+501609.1	52354-0875-583	18.07	16.650	16.238	15.600	0.787		
J104459.60+365605.1	53463-2090-329	16.81	15.537	15.157	14.331	0.701	y	
J105259.99+065358.0	52670-1001-080	18.56	-	-	-	0.722		
J105856.75+480805.4	52646-0964-305	18.00	16.539	15.965	15.313	0.591		y
J111628.00+434505.8	53061-1364-095	17.44	15.887	15.748	15.291	0.801		
J112526.12+002901.3	51614-0281-427	18.10	16.485	16.300	15.356	0.864	y	
J112621.25+343628.9	53713-2100-539	17.86	16.545	16.308	15.594	0.603		
J112822.42+482310.0	52642-0966-203	17.59	16.546	16.265	15.919	0.543		

Table 1—Continued

SDSS Name	Plate-MJD-Fiber <sup>a</sup>	r' Mag	J Mag <sup>c</sup>	H Mag <sup>c</sup>	K Mag <sup>c</sup>	z <sup>b</sup>	Fe II <sup>d</sup>	H $\beta$ <sup>e</sup>
J112828.31+011337.9	51992-0512-123	18.60	16.055	15.386	14.440	0.893	y	
J113807.83+531231.6	52367-0880-404	18.67	16.953	16.406	16.107	0.790		
J114043.62+532438.9	52734-1015-085	18.31	16.942	16.408	15.304	0.530		
J114209.01+070957.7	53383-1621-306	18.42	-	-	-	0.497		
J120751.48+253953.7	54484-2656-420	18.18	16.579	16.361	15.802	0.874		y
J121113.38+121937.3	53149-1612-179	18.60	16.764	15.894	14.893	0.464		y
J121303.40-014450.9	52367-0332-579	18.54	-	-	-	0.612		y
J121442.30+280329.1	53823-2229-557	17.38	15.790	15.649	14.594	0.695	y	
J123820.19+175039.1	54234-2599-503	16.42	15.326	14.285	12.957	0.453		y
J124300.87+153510.6	53502-1769-584	18.52	-	-	-	0.561	y	
J130741.12+503106.4	52753-1281-361	18.25	-	-	-	0.701		
J131433.19+471457.7	53062-1461-431	18.88	15.518	15.017	14.606	0.869		
J134415.75+331719.1	53503-2024-346	18.82	-	-	-	0.686	y	y
J134651.31+302421.7	53851-2094-598	18.44	-	-	-	0.867		

Table 1—Continued

SDSS Name	Plate-MJD-Fiber <sup>a</sup>	r' Mag	J Mag <sup>c</sup>	H Mag <sup>c</sup>	K Mag <sup>c</sup>	z <sup>b</sup>	Fe II <sup>d</sup>	H $\beta$ <sup>e</sup>
J140806.20+305448.4	53795-2125-236	17.41	16.090	15.646	14.993	0.830		
J142649.24+032517.7	52049-0584-004	8.37	16.723	16.015	15.176	0.530		
J142927.28+523849.5	52781-1327-343	17.51	16.257	15.585	14.845	0.594		
J144211.79+533608.5	52669-1163-293	18.67	-	-	-	0.863	y	
J144800.15+404311.7	53119-1397-198	17.09	15.118	14.903	14.322	0.801	y	
J145233.68+250002.6	54184-2143-603	18.50	-	-	-	0.587		
J145724.00+452157.8	53147-1676-449	18.62	17.094	16.074	15.447	0.717		
J145736.70+523454.6	52674-1164-184	18.08	-	-	-	0.637		
J145836.73+433015.5	52734-1290-601	18.59	16.926	16.630	15.491	0.761		
J150847.41+340437.7	53108-1385-173	17.35	15.690	15.696	14.859	0.798		y
J151306.52+200244.1	54525-2156-258	18.85	-	-	-	0.703	y	
J152350.42+391405.2	52765-1293-234	16.65	15.347	14.866	13.860	0.661		
J153209.51+061356.1	54540-1819-024	17.06	15.545	15.251	14.892	0.835		
J154351.92+162422.1	54243-2518-350	16.24	14.672	14.301	13.224	0.849		

Table 1—Continued

SDSS Name	Plate-MJD-Fiber <sup>a</sup>	r' Mag	J Mag <sup>c</sup>	H Mag <sup>c</sup>	K Mag <sup>c</sup>	z <sup>b</sup>	Fe II <sup>d</sup>	H $\beta$ <sup>e</sup>
J154620.98+453916.7	52782-1333-601	17.57	16.274	16.134	15.594	0.459		y
J160143.75+150237.7	54568-2524-356	17.26	15.772	15.638	14.587	0.650	y	y
J160234.88+160041.1	53555-2197-225	18.18	-	-	-	0.719		
J160656.95+133931.2	54569-2527-346	18.67	-	-	-	0.452		y
J161637.15+390356.8	52759-1336-088	17.90	16.970	16.333	15.344	0.810		
J162435.28+090731.6	54589-2532-378	18.06	16.547	15.936	14.949	0.652		y
J163255.46+420407.8	52379-0816-569	18.68	-	-	-	0.726	y	y
J163656.84+364340.4	52782-1174-337	18.91	17.013	16.251	15.719	0.850		
J164447.19+311437.2	52781-1340-002	17.90	16.369	16.115	15.281	0.690		
J170010.82+395545.8	52079-0633-482	18.99	17.240	16.463	15.641	0.577		y
J170341.82+383944.7	52071-0632-632	18.72	16.795	15.999	15.426	0.554		y
J204333.20-001104.2	52435-0981-044	17.94	16.793	15.769	15.223	0.545		
J210757.67-062010.6	52174-0637-610	17.22	15.732	15.082	14.145	0.642	y	y
J220931.92+125814.5	52519-0735-501	18.52	-	-	-	0.813		y

Table 1—Continued

---



---

SDSS Name	Plate-MJD-Fiber <sup>a</sup>	r' Mag	J Mag <sup>c</sup>	H Mag <sup>c</sup>	K Mag <sup>c</sup>	z <sup>b</sup>	Fe II <sup>d</sup>	H $\beta$ <sup>e</sup>
-----------	------------------------------	--------	--------------------	--------------------	--------------------	----------------	--------------------	------------------------

---



---

<sup>a</sup>The corresponding SDSS plate number, modified julian date, and fiber number for the object.

<sup>b</sup>redshift of the object.

<sup>c</sup>IR magnitudes from 2MASS.

<sup>d</sup>Absorption troughs from Fe II detected at similar velocities to Mg II.

<sup>e</sup>BALs with narrow H $\beta$  emission lines.

Table 2. LoBAL Reddening Determinations

SDSS Name	$E(B-V)_{MW}$	$E(B-V)_Q$	$E(B-V)_{NLR}$
FeLoBALs			
0149–1016 <sup>a</sup>	0.038	0.11±0.03	0.15±0.15
0802+5513	0.042	0.35±0.05	0.62±0.26
0806+1150	0.022	0.10±0.11	–
1032+0835	0.021	0.08±0.07	–
1044+3656	0.013	0.05±0.04	–
1125+0029	0.031	0.11±0.09	–
1128+0113	0.029	0.10±0.10	–
1214+2803	0.021	0.08±0.07	–
1243+1535	0.032	0.00±0.10	–
1344+3317	0.014	0.20±0.10	>0.23
1442+5336	0.009	-0.05±0.05	–
1448+4043	0.011	-0.02±0.09	–
1513+2002	0.032	0.11±0.05	–
1601+1502	0.042	0.06±0.04	–
1632+4204	0.025	0.11±0.09	– <sup>b</sup>
2107–0620	0.058	0.14±0.05	>0.18
LoBALs			
0103+0037	0.029	0.13±0.06	–

Table 2—Continued

SDSS Name	$E(B-V)_{MW}$	$E(B-V)_Q$	$E(B-V)_{NLR}$
0242–0853	0.022	$0.03 \pm 0.07$	$0.06 \pm 0.28$
0809+2548	0.032	$-0.02 \pm 0.09$	$> -0.05$
0822+2311	0.034	$0.00 \pm 0.03$	$> -0.07$
0835+4352	0.028	$0.00 \pm 0.04$	–
0850+4451	0.024	$-0.03 \pm 0.07$	–
0853+4633	0.021	$0.00 \pm 0.03$	–
0925+2021	0.038	$-0.05 \pm 0.15$	–
0932+5553	0.025	$0.15 \pm 0.05$	–
0933+3519	0.012	$0.00 \pm 0.10$	$-0.06 \pm 0.18$
0942+5656	0.017	$0.06 \pm 0.04$	–
0944+0625	0.026	$0.03 \pm 0.03$	–
1010+1843	0.027	$0.11 \pm 0.03$	$0.09 \pm 0.28$
1017+2641	0.023	$0.00 \pm 0.10$	$> 0.03$
1028+5929	0.007	$0.00 \pm 0.10$	–
1030+3120	0.018	$0.00 \pm 0.05$	–
1041–0056	0.046	$-0.10 \pm 0.03$	$0.14 \pm 0.16$
1042+5016	0.013	$0.03 \pm 0.05$	–
1052+0653	0.033	$0.00 \pm 0.09$	–
1058+4808	0.011	$-0.02 \pm 0.04$	$0.18 \pm 0.14$
1116+4345	0.013	$0.06 \pm 0.04$	–



Table 2—Continued

SDSS Name	$E(B-V)_{MW}$	$E(B-V)_Q$	$E(B-V)_{NLR}$
1126+3436	0.022	$-0.03 \pm 0.03$	—
1128+4823	0.017	$0.05 \pm 0.04$	—
1138+5312	0.007	$0.11 \pm 0.09$	—
1140+5324	0.009	$-0.05 \pm 0.15$	—
1142+0709	0.034	$0.00 \pm 0.10$	—
1207+2539	0.018	$0.05 \pm 0.05$	$0.03 \pm 0.19$
1211+1219	0.025	$0.06 \pm 0.14$	$0.13 \pm 0.26$
1213–0144	0.020	$0.03 \pm 0.04$	$0.27 \pm 0.21$
1238+1750	0.021	$-0.04 \pm 0.04$	$-0.05 \pm 0.12$
1307+5031	0.013	$0.08 \pm 0.07$	—
1314+4714	0.009	$0.03 \pm 0.07$	—
1346+3024	0.017	$0.00 \pm 0.03$	—
1408+3054	0.009	$0.05 \pm 0.05$	—
1426+0325	0.031	$-0.02 \pm 0.07$	—
1429+5238	0.012	$0.02 \pm 0.08$	—
1452+2500	0.030	$-0.03 \pm 0.13$	—
1457+4521	0.015	$0.02 \pm 0.05$	—
1457+5234	0.016	$-0.10 \pm 0.11$	—
1458+4330	0.014	$0.08 \pm 0.12$	—
1508+3404	0.014	$0.06 \pm 0.04$	$-0.19 \pm 0.17$

Table 2—Continued

SDSS Name	$E(B-V)_{MW}$	$E(B-V)_Q$	$E(B-V)_{NLR}$
1523+3914	0.018	$0.04 \pm 0.03$	–
1532+0613	0.042	$0.02 \pm 0.03$	–
1543+1624	0.028	$0.06 \pm 0.04$	–
1546+4539	0.013	$0.00 \pm 0.10$	$-0.05 \pm 0.24$
1602+1600	0.028	$0.02 \pm 0.05$	–
1606+1339	0.036	$0.03 \pm 0.12$	$0.02 \pm 0.12$
1616+3903	0.007	$0.00 \pm 0.10$	–
1624+0907	0.057	$0.00 \pm 0.10$	$0.02 \pm 0.90$
1636+3643	0.012	$0.10 \pm 0.10$	–
1644+3114	0.024	$0.23 \pm 0.07$	–
1700+3955	0.020	$0.16 \pm 0.14$	$0.59 \pm 0.30^d$
1703+3839	0.036	$0.40 \pm 0.40$	$>0.2$
2043–0011	0.056	$-0.02 \pm 0.08$	–
2209+1258	0.072	$0.05 \pm 0.05$	$>-0.09$

<sup>a</sup>Object also has  $H\alpha$ . This ratio is between  $H\beta$  to  $H\alpha$ .

<sup>b</sup>Object has no uncontaminated O III emission tem-

plate available.

<sup>c</sup>Spectrum too noisy for accurate measurement.

<sup>d</sup>Used  $H\beta$  for line template.

Table 3. Reddening Statistics

$E(B-V)_Q$ Range	LoBAL %
$E(B-V) < -0.10$	0.0
$-0.10 \geq E(B-V) < -0.05$	7.1
$-0.05 < E(B-V) < 0.05$	48.6
$0.05 < E(B-V) < 0.09$	25.7
$E(B-V) \geq 0.10$	22.9

## REFERENCES

- Antonucci, R. R. J., & Miller, J. S. 1985, *ApJ*, 297, 621
- Barlow, T. A., & Sargent, W. L. W. 1997, *AJ*, 113, 136
- Bautista, M. A., Dunn, J. P., Arav, N., Korista, K. T., Moe, M., & Benn, C. 2010, *ApJ*, 713, 25
- Becker, R. H., Gregg, M. D., Hook, I. M., McMahon, R. G., White, R. L., & Helfand, D. J. 1997, *ApJ*, 479, L93
- Bernstein, R., Shectman, S. A., Gunnels, S. M., Mochnacki, S., & Athey, A. E. 2003, in *Society of Photo-Optical Instrumentation Engineers (SPIE) Conference Series*, Vol. 4841, *Society of Photo-Optical Instrumentation Engineers (SPIE) Conference Series*, ed. M. Iye & A. F. M. Moorwood, 1694–1704
- Borguet, B. C. J., Arav, N., Edmonds, D., Chamberlain, C., & Benn, C. 2013, *ApJ*, 762, 49
- Boroson, T. A., & Green, R. F. 1992, *ApJS*, 80, 109
- Dawson, K. S. et al. 2013, *AJ*, 145, 10
- Debuhr, J., Quataert, E., Ma, C.-P., & Hopkins, P. 2010, *MNRAS*, 406, L55
- Di Matteo, T., Springel, V., & Hernquist, L. 2005, *Nature*, 433, 604
- Dubois, Y., Gavazzi, R., Peirani, S., & Silk, J. 2013, *MNRAS*, 433, 3297
- Dunn, J. P. et al. 2010, *ApJ*, 709, 611
- Egami, E., Iwamuro, F., Maihara, T., Oya, S., & Cowie, L. L. 1996, *AJ*, 112, 73
- Faucher-Giguère, C.-A., Quataert, E., & Murray, N. 2012, *MNRAS*, 420, 1347

- Glikman, E. et al. 2012, ApJ, 757, 51
- Greene, J. E., & Ho, L. C. 2005, ApJ, 630, 122
- Hall, P. B. et al. 2002, ApJS, 141, 267
- Heckman, T. M., Miley, G. K., van Breugel, W. J. M., & Butcher, H. R. 1981, ApJ, 247, 403
- Hewett, P. C., & Foltz, C. B. 2003, AJ, 125, 1784
- Hopkins, P. F., Hernquist, L., Cox, T. J., & Kereš, D. 2008, ApJS, 175, 356
- Hopkins, P. F., Kereš, D., & Murray, N. 2013, MNRAS, 432, 2639
- Hopkins, P. F. et al. 2004, AJ, 128, 1112
- Knigge, C., Scaringi, S., Goad, M. R., & Cottis, C. E. 2008, MNRAS, 386, 1426
- Komossa, S., Xu, D., Zhou, H., Storchi-Bergmann, T., & Binette, L. 2008, ApJ, 680, 926
- Korista, K. T., Bautista, M. A., Arav, N., Moe, M., Costantini, E., & Benn, C. 2008, ApJ, 688, 108
- Korista, K. T., & Goad, M. R. 2004, ApJ, 606, 749
- Kwan, J., & Krolik, J. H. 1981, ApJ, 250, 478
- Maiolino, R., Marconi, A., & Oliva, E. 2001, A&A, 365, 37
- Mathews, W. G., & Ferland, G. J. 1987, ApJ, 323, 456
- Moe, M., Arav, N., Bautista, M. A., & Korista, K. T. 2009, ApJ, 706, 525
- Osterbrock, D. E., & Ferland, G. J. 2006, Astrophysics of gaseous nebulae and active galactic nuclei, ed. Osterbrock, D. E. & Ferland, G. J.

- Ostriker, J. P., Choi, E., Ciotti, L., Novak, G. S., & Proga, D. 2010, *ApJ*, 722, 642
- Peterson, B. M. 1997, *An Introduction to Active Galactic Nuclei (An introduction to active galactic nuclei, Publisher: Cambridge, New York Cambridge University Press, 1997 Physical description xvi, 238 p. ISBN 0521473489)*
- Reichard, T. A. et al. 2003, *AJ*, 126, 2594
- Reynolds, C. S., Ward, M. J., Fabian, A. C., & Celotti, A. 1997, *MNRAS*, 291, 403
- Richards, G. T. et al. 2003, *AJ*, 126, 1131
- Schlafly, E. F., & Finkbeiner, D. P. 2011, *ApJ*, 737, 103
- Schneider, D. P. et al. 2010, *AJ*, 139, 2360
- Silk, J., & Nusser, A. 2010, *ApJ*, 725, 556
- Silk, J., & Rees, M. J. 1998, *A&A*, 331, L1
- Skrutskie, M. F. et al. 1997, in *Astrophysics and Space Science Library*, Vol. 210, *The Impact of Large Scale Near-IR Sky Surveys*, ed. F. Garzon, N. Epchtein, A. Omont, B. Burton, & P. Persi, 25
- Sprayberry, D., & Foltz, C. B. 1992, *ApJ*, 390, 39
- Trippe, M. L., Crenshaw, D. M., Deo, R. P., Dietrich, M., Kraemer, S. B., Rafter, S. E., & Turner, T. J. 2010, *ApJ*, 725, 1749
- Urrutia, T., Becker, R. H., White, R. L., Glikman, E., Lacy, M., Hodge, J., & Gregg, M. D. 2009, *ApJ*, 698, 1095
- Urrutia, T., Lacy, M., & Becker, R. H. 2008, *ApJ*, 674, 80
- Urry, C. M., & Padovani, P. 1995, *PASP*, 107, 803

Vanden Berk, D. E. et al. 2001, *AJ*, 122, 549

Weymann, R. J., Morris, S. L., Foltz, C. B., & Hewett, P. C. 1991, *ApJ*, 373, 23

White, R. L. et al. 2000, *ApJS*, 126, 133

Zhang, S., Wang, T.-G., Wang, H., Zhou, H., Dong, X.-B., & Wang, J.-G. 2010, *ApJ*, 714,  
367